Dynamic Characteristics of Regional Flows around the Pyrénées in View of the PYREX Experiment. Part II: Solution of a Linear Model Compared to Field Measurements

E. KOFFI AND B. BÉNECH

Laboratoire d'Aerologie, Universite Paul Sabatier, Toulouse, France

J. STEIN

Centre National de Recherches Meteorologiques, Meteo-France, Toulouse, France

B. TERLIUC

Department of Environmental Researches, Nuclear Research Centre, Negev, Israel

(Manuscript received 29 July 1996, in final form 10 February 1997)

ABSTRACT

This paper considers a linear hydrostatic model of a stable, uniform, constant rotational airflow over three-dimensional, elliptic, cross-sectional families of mountains in a *z* system. The surface pressure and the winds that are induced around the mountain chain are deduced using Fourier representation in both horizontal directions. The surface pressure perturbations and the induced wind intensities are linked to 1) the incoming airmass thermodynamic properties through Froude and Rossby numbers, 2) the geometrical aspect ratio of the mountain, 3) the direction of incidence of the incoming flow relative to the mountain orientation, and 4) the Coriolis effect through the Rossby number. The balance between the different factors that contribute to the morphology of the pressure and wind fields was established for northerly and southerly incoming flows that were blocked by an elliptical barrier resembling the Pyrénées mountain chain. Fair agreement was found between the results of the model and the experimental data collected during PYREX (Pyrénées experiment) intensive operational periods, with special regard to the asymmetry of the lateral flow for northerly incoming air masses.

1. Introduction

Regional winds generated around the Pyrénées range were found to be well related to surface pressure perturbations, earth rotation, and upwind direction of incidence (DI) (Bénech et al. 1998). Rossby numbers varying in the range $0.5 < \mathrm{Ro} < 5$ and low Froude number values (i.e., $\mathrm{Fr} < 0.5$), measured during 10 intensive operational periods (IOPs) of the Pyrénées experiment (PYREX), are located in the sector of the diagram of Pierrehumbert and Wyman (1985) for which important nonlinear upstream-blocking and splitting effects are expected to affect the flow in the vicinity of the Pyrénées range (Bénech et al. 1998; their Table 1 and Fig. 5). Moreover, air masses having relatively low Rossby numbers, as documented in PYREX, are expected to be affected by the earth's rotation, and the Coriolis effect will yield an asymmetric splitting of the airstream, with stronger velocities on the left edge than on the right edge of the mountain. This asymmetry can be enhanced or counterbalanced by the synoptic-driven wind, depending on its direction. Thus, during northerly synoptic flows, tramontane winds observed on the eastern flank of the Pyrénées were considerably stronger than cierzo winds on the eastern edge (see Bénech et al. 1998; their Figs. 13a, 13b, and 14a). During southerly flows, the asymmetry was very weak, resulting in bochorno (west side) and marin–autan (east side) winds, blowing at almost the same velocities (Bénech et al. 1998; their Figs. 13c, 13d, and 14b).

Low Froude number airflows around obstacles are complex, even when idealized in laboratory and numerical studies. Beyond pure dynamic considerations, thermal effects, friction at boundary layers, terrain complexity, nonuniformity of dynamic, and thermodynamic and moisture profiles complicate the problem even further.

Linear solutions of the equations of motion, developed by Lyra (1943) and Queney (1948) to describe the flow perturbation induced by a two-dimensional barrier, were extended by Wurtele (1957) to study the three-dimensional wave motion of uniform flow in the far field of an obstacle. Drazin (1961) showed in a theoretical study that highly stable flows are almost com-

Corresponding author address: Dr. B. Benech, Centre de Recherches Atmospheriques, 65300 Lannemezan, France.
E-mail: benb@aero.obs-mip.fr

pletely split by three-dimensional obstacles. The results achieved by Drazin (1961) should be considered conceptually controversial, regarding the capability of the linear theory to describe blocked flow features like splitting and stagnation because they are, in fact, nonlinear effects involving perturbations of the same magnitude as the average characteristics of the incoming flow.

Wave breaking, collapse of density surfaces, flow splitting, and stagnation are all nonlinear effects predicted by the linear theory, which can also provide clear criteria for the occurrence of such anomalies (Smith 1979, 1980, 1988; Phillips 1984). For instance, Smith (1980) showed that the small perturbation assumption, used to linearize the equations of motion of a stratified Bussinesq fluid over an isolated obstacle, is no longer rigorously valid in front of the obstacle for Froude numbers smaller than one, as the first stagnation of the flow appears; on the lee side, nonlinear wake effects are presents when the Froude number decreases to two.

In spite of the conceptual contradictions and inaccuracies that affect the solution of the linearized equations for small Froude numbers, many attempts have been made to extrapolate the linear theory toward dynamic systems for which nonlinear effects are expected to be large.

Extensive applications of the solution of the linear equations of motion, some of them implementing the Fourier transform technique, were directed to describe neutral (Taylor et al. 1983; Mason and King 1985; Beljaars et al. 1987) and stable (Hunt et al. 1988) stratified boundary layer airflows passing over low hills. While some of the studies included friction, rotational effects due to the Coriolis force were not accounted for in view of the reduced dimensions of the obstacles. Klemp and Lilly (1975) used a linear model to determine some criteria for the occurrence or inhibition of a strong downslope wind in the Colorado Rockies. Comparative studies of solutions derived from the linear theory and from nonlinear two-dimensional models have shown good agreement in many cases (Klemp and Lilly 1978). Moreover, several studies (Buzzi and Tibaldi 1977; Vergeiner 1971; Somieski 1981; Smith 1982) have shown that the linear theory can be successfully used in studies of some basic mechanisms of the low layer's flow around mountains. Phillips (1984) developed a linear solution of the equations of motion to describe the flow perturbation due to an elliptical barrier and its dependence on the direction of incidence of the incoming air mass. The series expansion of the density surfaces given by Smith's (1988) linear model in isosteric coordinates were shown to be rigorously correct at any point (x, y, z_0) for which $z_0 < 0.5\mathrm{Fr}H$ (Bénech et al. 1998) (Fr is the Froude number of the flow and H is the height of the circular, bell-shaped hill) and inaccurate in the wake of the hill, where the series converge poorly (Smith 1988). The validity of the solution and the extent of the inaccuracies should be finally assessed by numerical and experimental tests.

Some simulations of stable, stratified, three-dimensional airflow around a circular topographic barrier, using the nonlinear limited-area PERIDOT (Prévision à Echéance Rapprochèe Intègrant des Données Observées et Tèlèdèteetèes) model (Imbard et al. 1986; Bougeault et al. 1991), have been conducted by Stein (1992). A comparative analysis of the results demonstrates that the linear theory can be modified to describe the windward and lateral flow around the obstacle for relatively small Froude numbers. Encouraged by these results and motivated by the relative simplicity that numerical models based on the linearized equations of motion can be implemented in pure and applied research and operational tasks, we assessed the applicability of the linear theory to analyze the data collected in the PYREX experiment around the Pyrénées, even in the event that the flow is blocked.

As pointed out in Part I (Bénech et al. 1998), the framework for the development of our study is subjected to the methodology used in mathematics when a statement ''if and only if'' is to be proved. Therefore, the link between the PYREX experimental results and the linear theory is presented in two parts. Part I is related to the formation of the regional winds in the flanks of the Pyrénées to the incoming air masses, characterized by Froude and Rossby numbers and the DI of the undisturbed mean wind, and to the perturbed pressure field. Then, using the Froude number as the key tool, the experimental results were used to assess some of the predictions of the extrapolation of the linear theory to the cases under study, in view of its explicit role in some expressions derived from the manipulation of the linearized equations. Part II is the reciprocal step required to accomplish our methodology. Following the theoretical works of Smith (1980) and Phillips (1984) that dealt with particular cases of airflow around isolated obstacles, we developed an integrated linear model that takes into account the Coriolis effect, the DI, and the elliptic shape of the mountain range that resembles the Pyrénées, and that can be easily implemented for numerical calculations. Instead of using the Froude number as in Part I, in Part II the Rossby number is found to be more appropriate to study the variations of the total pressure and wind intensity fields due to its close connection to the Coriolis effect. The model is used to estimate the pressure field in the vicinity of the mountain and the specific contributions of the DI and the Coriolis effect to the asymmetry of the flow. Then, the linear model capability to explain the main features of blocked airflow with a relatively low Froude number, in front of and in the flanks of the elliptic mountain, is tested by comparing numerical simulation results to the data measured during the PYREX experiment, when induced winds were developed. As pointed out in Part I, the analysis of the deviations from the main features in some cases is left out of the scope of this work, and only occasional attention will be dedicated to the characteristics of the flow that are not expressed by Rossby and

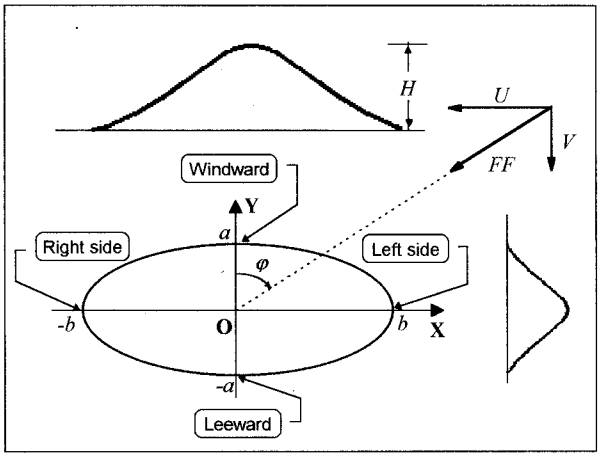

FIG. 1. Schematic representation of the incoming airflow (FF) over a topographic elliptical barrier used in the development of the linear model. The labels indicating the sides of the barrier apply to the direction of FF.

Froude numbers and incoming wind velocity and direction. The application of a rigorous methodology is only schematic and dedicated to providing a suitable framework for the presentation of the topic.

2. Numerical linear model

a. Geometry of the system

A 3D Cartesian coordinate system is attached to the topographic obstacle at mean sea level (MSL). The horizontal cross sections of the obstacle are idealized by ellipsoids centered at $z = 0$. At ground level, the lengths of the principal and secondary axis, oriented in the X and Y directions, are $2b$ and $2a$, respectively (Fig. 1). The aspect ratio of horizontal scaling lengths is defined as

$$\gamma = a/b. \tag{1}$$

The topographic barrier is idealized by a 3D, elliptical, bell-shaped mountain, defined by the analytical expression

$$h(x, y) = \frac{H}{[1 + (x/b)^2 + (y/a)^2]^{\mu}}, \tag{2}$$

where H is the mountaintop height, and the exponent μ in Eq. (2) specifies the rate of variation of the terrain level.

The incoming wind components in the X and Y directions, which are parallel and normal to the principal axis of the mountain, will be represented by U and V, respectively. By convention, angles are measured clockwise from the positive direction of the OY axis. The DI φ of the incoming flow is the angle of the vector pointing to the incoming direction of the flow and is defined by

$$\varphi = \arctan\left(\frac{U}{V}\right). \tag{3}$$

The designations of the right side and left side of the mountain are referred to the direction of the component of the incoming airflow, perpendicular to the mean axis of the mountain range. Therefore, the right side of the mountain for northerly flows is the west side, and the east side for southerly flows, as shown in Fig. 1.

b. The system of equations and their solution

Following Smith (1980, 1982) and Phillips (1984), the earth's rotation and DI effects are introduced in the equations of motion through a uniform Coriolis parameter f and the horizontal wind components U and V, respectively. Roughness effects are neglected. The perturbations to the incoming wind components U, V, and $W \equiv 0$, background mean air pressure p and density ρ, are u', v', w', p', and ρ', respectively. Ignoring second-order terms, the linearized equations for an inviscid, steady, hydrostatic flow are (Koffi 1994)

$$\rho U\frac{\partial u'}{\partial x} + \rho V\frac{\partial u'}{\partial y} + \frac{\partial p'}{\partial x} - \rho f v' = 0, \tag{4}$$

$$\rho U\frac{\partial v'}{\partial x} + \rho V\frac{\partial v'}{\partial y} + \frac{\partial p'}{\partial y} + \rho f u' = 0, \tag{5}$$

$$\frac{\partial p'}{\partial z} - \rho' g = 0, \tag{6}$$

and

$$\rho\left(\frac{\partial u'}{\partial x} + \frac{\partial v'}{\partial y} + \frac{\partial w'}{\partial z}\right) = 0. \tag{7}$$

The system comprises three equations of motion [Eqs. (4)–(6)] and the continuity equation [Eq. (7)]. The main steps followed in the solution of the linearized system are described in the appendix.

c. Parameters involved in the numerical simulations

For simple obstacles like a circular hill ($\gamma = 1$), the solutions of the system of Eqs. (4)–(7) can be analytical. For elliptical mountains [Eq. (2)] having $\gamma \neq 1$, a numerical method should be applied. Smith (1980, 1982) analyzed the airflow over a bell-shaped hill with $\gamma = 1$ and a variety of Fr and Ro ≥ 5. Phillips (1984) and Smith (1989) derived solutions for airflows with a constant Rossby number (Ro $= \infty$) and variable Fr over families of ellipsoidal hills. Buzzi and Tibaldi (1977) determined analytical solutions for airflows with low Froude and Rossby numbers (i.e., Fr and Ro $\ll 1$) over a bell-shaped circular hill ($\gamma = 1$, $\mu = 3/2$). The numerical experiments described in the present work reviewed all the configurations mentioned above.

The Fourier analysis in the present work is performed at equally spaced horizontal wave numbers k and l, defined by

$$k = \frac{2\pi}{L_x} N_k \tag{8}$$

and

$$l = \frac{2\pi}{L_y} N_l \tag{9}$$

where the integer numbers vary in the ranges $0 \leq N_k \leq L_x/\Delta x$ and $0 \leq N_l \leq L_y/\Delta y$, such that L_x and L_y are the largest wavelengths used in the spectral representation of the solution that, in the present case, are the size of the computational domain in the X and Y directions. Double Fourier transforms are computed using the software MATLAB 4.1 double Fourier transform routine on a 486 PC. Following Phillips (1984), the spectral solutions of the perturbations p', u', and v' at ground level are expressed in elliptical coordinates, as shown in the appendix, for incoming flow at normal incidence ($\varphi = 0$).

The geometrical parameters γ, μ, and h required to idealize the Pyrénées range by a 3D elliptical obstacle described by Eq. (2) were determined from the analysis of geographical topographic maps. Roughly, the Pyrénées range can be depicted as a barrier oriented in the west–east direction, with a 40- to 80-km width, 40-km length, and 3000 m MSL height in its central part (Bénech et al. 1998; their Fig. 1). Several cross sections were examined to account for the spatial variability of the mountain range: three north–south cross sections and three west–east cross sections, shown in Fig. 2a and 2b, respectively. The different north–south and west–east cross sections of the Pyrénées range were best fitted by Eq. (2) with $H = 3000$ m, $a = 40$ km, $b = 200$ km, $\gamma = 40/200 = 1/5$, and $\mu = 1$.

3. Pressure dipole and deflected wind modelization, accounting for the Coriolis and DI effects

a. Description of input parameters

The variability of the wind fields obtained with different values of μ was not found to be significant when compared to the dependence on γ, namely, only the maximal pressure perturbation moves toward the mountaintop when μ increases. Consequently, the slope parameter will be kept constant with value $\mu = 3/2 = 1.5$. The half-width of the simulation barrier will be kept constant, with value $a = 40$ km, to match the equivalent size of the Pyrénées. Two values of the aspect ratio will be considered: $\gamma = 1$ and $\gamma = 1/5 = 0.2$ for circular and elliptical horizontal cross sections, respectively. Consequently the half-length b of the principal axis of the ellipsoid will take the values 40 and 200 km, respectively. The mountaintop height in the present simulation is equal to 3000 m MSL to match the top height of the Pyrénées.

The Rossby number [Eq. (A25)] in this analysis varies from 0.1 to ∞, which includes the variation range of $0.5 \leq \text{Ro} \leq 5$ found in PYREX (Bénech et al. 1998). Since the normal component of the incoming wind is kept constant and equal to 10 m s^{-1} along the present section, the variation of Ro can be attributed to the Coriolis parameter f. This is to accomplish one of the objectives of Part II—to test the sensibility of the model to the Coriolis effect.

Three upwind DI are applied: $\varphi = 0°$, 45°, and −45°. Due to the center symmetry of the barrier, the values of $\varphi = 0°$ represent pure northerly and pure southerly flows ($\varphi = 180°$), the value of $\varphi = -45°$ is representative of northwesterly and southeasterly ($\varphi = 135°$) flows, and $\varphi = 45°$ is representative of northeasterly and southwesterly ($\varphi = 225°$) flows. The angles that differ from normal incidence correspond to PYREX measurements, which show that the DIs during northerly flows were distributed around −45°, and during southerly flows around 200° (Bénech et al. 1998).

The Froude number [Eq. (A26)] was fixed along all the simulations to the value 0.33, which is the mean value encountered during PYREX (Bénech et al. 1998; their Table 1). Since the normal component of the incoming wind was kept constant in all the simulations ($V = 10$ m s^{-1}), this was accomplished by fixing the Brunt–Väisälä frequency to the value 0.01 s^{-1}, corresponding to a stable troposphere.

b. Description of output parameters

The output includes the following surface pressure and wind information.

- The surface pressure perturbation in terms of the dimensionless surface pressure perturbation $Cp(x, y)$ used by Smith (1980) and Phillips (1984) is defined as

$$Cp(x, y) = \frac{p'(x, y, 0)}{\rho N H \text{FF}}, \tag{10}$$

  where FF is the upstream wind modulus.
- The parallel $u'(x, y)$ and normal $v'(x, y)$ components of the wind velocity perturbations are defined with respect to the principal axis of the mountain.
- The surface total wind velocity modulus defined as

$$F(x, y) = \sqrt{[U + u'(x, y)]^2 + [V + v'(x, y)]^2}. \tag{11}$$

- The surface total wind velocity field will be represented in vector format.

c. Preliminary estimation of the limit of validity of the linear model

The analysis of Bénech et al. (1998) of the limitation of the validity of the series expansion of the solution of the linear equations of motion in isosteric coordinates given by Smith (1988) can be applied to obtain a preliminary estimation of the depth of the layer adjacent to ground level; the linear theory is rigorously valid in

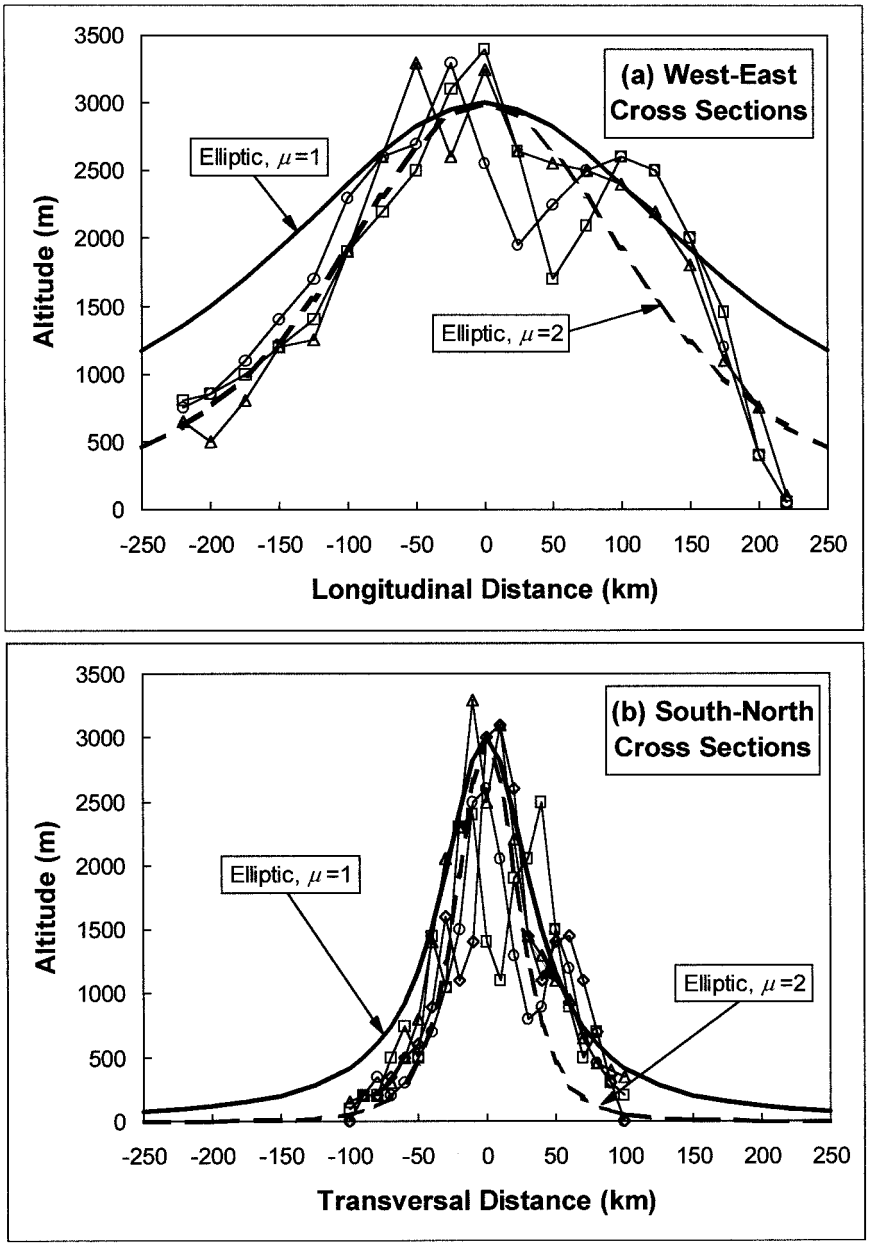

FIG. 2. Vertical smoothed cross sections of the Pyrénées range (marked solid lines) that were examined to account for its silhouette: (a) three in the west–east direction and (b) four in the north–south directions. The two elliptic model curves that best fit the whole shape of the mountain are drawn with unmarked lines and indicated by labels.

front of the topographic barrier for the cases to be solved hereafter. By introducing in the inequality $z_0 < 0.5\text{Fr}\,H$, the values Fr = 0.33 and H = 3000 m, to be used in the next sections will yield a depth of 500 m for the mentioned layer. As pointed out in the introduction, the validity of this estimation should be tested by experimental or numerical means. Meanwhile, it is interpreted as a formal justification to extend the use of our linear model to study low Froude number blocked flows at ground level in front of and in the flanks of the mountain.

d. The circular cross-sectional mountain ($\gamma = 1$)

The model was initially applied to a circular cross-sectional mountain to asses its applicability by comparison with the results of previous works. In the absence of the Coriolis effect (Ro = ∞), the dipolelike

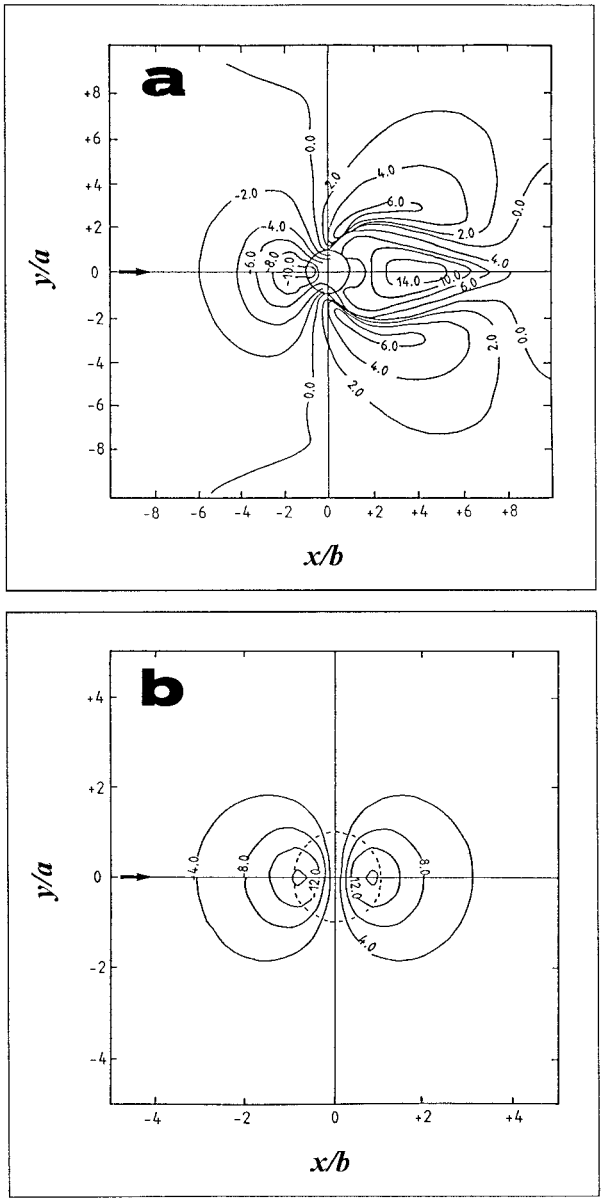

FIG. 3. The normal components of the wind perturbation at ground level in the vicinity of a circular hill simulated by (a) the 3D, nonlinear, hydrostatic model PERIDOT (after Stein 1992) and (b) the linear model for Fr = 0.22. Both cases are for large Rossby number (no rotational effect).

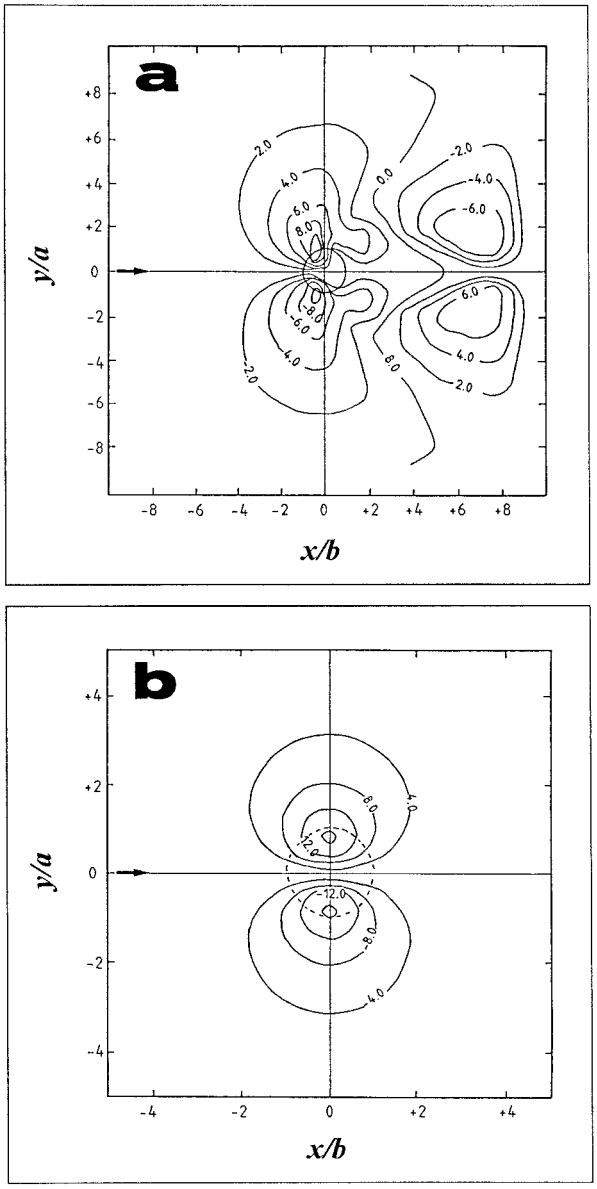

FIG. 4. As in Fig. 3 except for the parallel component of the wind.

morphology and the intensities of the pressure field were similar to those reported by Smith (1980) and Phillips (1984). For Ro = 0.5, the pressure dipole degenerates into a single high pressure system centered near the top of the mountain, which is in general agreement with the results of Buzzi and Tibaldi (1977).

The basis for the validation of the wind field calculated with the linear model was chosen to be the results obtained by Stein (1992) using the 3D, nonlinear, hydrostatic model PERIDOT to simulate the flow over a circular hill that is characterized by a low Froude number (Fr = 0.22) and a large Rossby number (without the Coriolis effect). The structure of the normal and the parallel components of the wind perturbation at ground level is demonstrated in Fig. 3a and 4a for the nonlinear simulation and in Figs. 3b and 4b for the linear simulation, respectively. For this particular comparison, the linear model was run with Fr = 0.22 as well. The morphology and the intensities of the wind fields obtained with the two models are almost identical in front of the mountain. The large differences are found in the lee side, where the downwind mirror image symmetry predicted by the 3D linear solution is replaced by the vortex generated by the nonlinear model. It can be inferred from this comparison that, even for low Froude num-

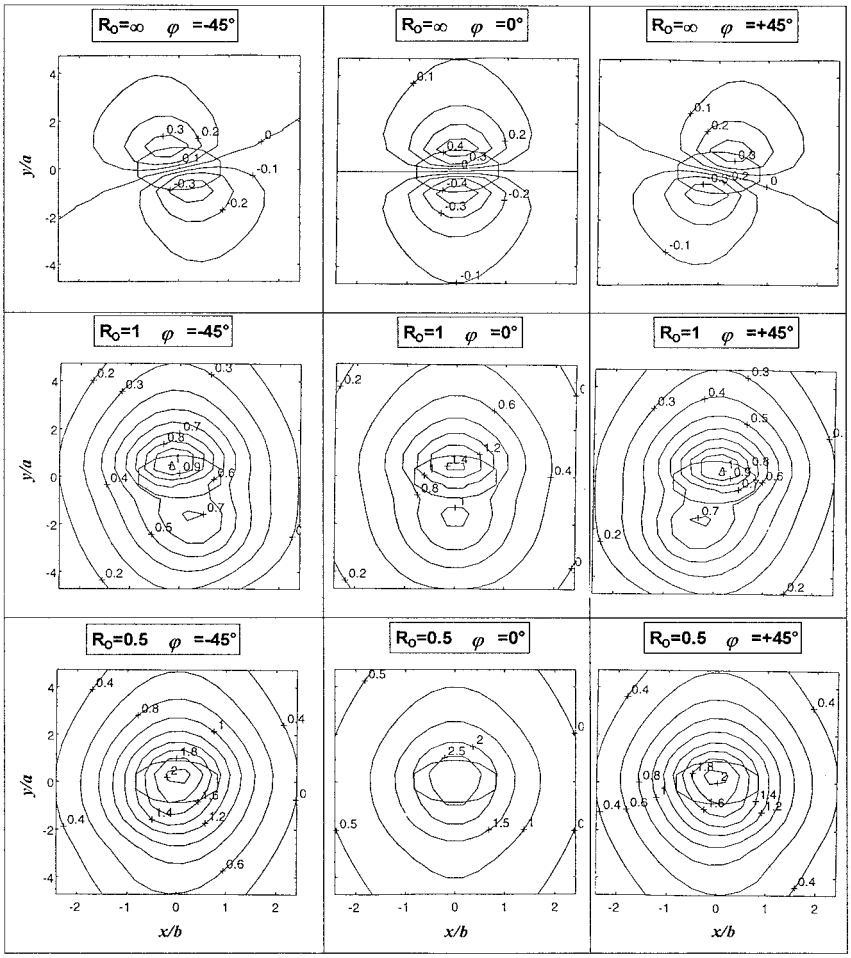

FIG. 5. The dimensionless pressure coefficient field $Cp(x, y)$ around an elliptical ($\gamma = 1/5$) barrier, induced by uniform airflows characterized by Rossby numbers Ro $= \infty$ (Coriolis effect absent) (upper row), Ro $= 1$ (midrow) and Ro $= 0.5$ (lower row), DI $\varphi = -45°$ (left column), $\varphi = 0°$ (midcolumn), and $\varphi = +45°$ (right column).

bers, the large features of the flow structure in the upstream side of the mountain can be explained by the linear theory. In this context, there is a particular interest to analyze the factors contributing to the asymmetric flow on the two edges of the mountain, as were encountered during PYREX (Bénech et al. 1998). The study of the influence of the DI and the Coriolis effect on the asymmetry of the flow around the obstacle is expected to be simpler when conducted with a linear model and can be realistic when compared with experimental data.

e. The elliptical cross-sectional barrier ($\gamma = 1/5$)

1) PRESSURE PERTURBATION FIELD

For all the DI and for Ro $= \infty$, the pressure perturbation fields have a bipolar nature, as can be seen in Fig. 5. When Ro decreases (enhancement of the Coriolis effect), the pressure dipole degenerates into an high pressure system, almost in the same way as in the circular case. The continuous variations of the pressure perturbation fields as a function of Ro, for $\varphi = 0°$ and $\pm 45°$ at the particular points $(0, a)$ and $(0, -a)$, are given in Fig. 6, the elliptical barrier. These particular points, located the line that overlaps the instrumented transect assigned to measure the pressure drag (Bénech et al. 1998), were chosen by considering that the difference between the pressure perturbation at their locations will indicate the intensity of the blocking effect. Indeed, the figure provides a quantitative description of the general tendency of the pressure values to increase on both sides of the mountain when Ro decreases. Simultaneously, the pressure difference decreases, until the pressure dipole degenerates to a bimodal high pressure system, when Ro $= 3$ (Ro $= 2$ for the circular shape). Further, the bimodal characteristic degenerates into a single high pressure system for Ro smaller than 0.5. These pressure field variations

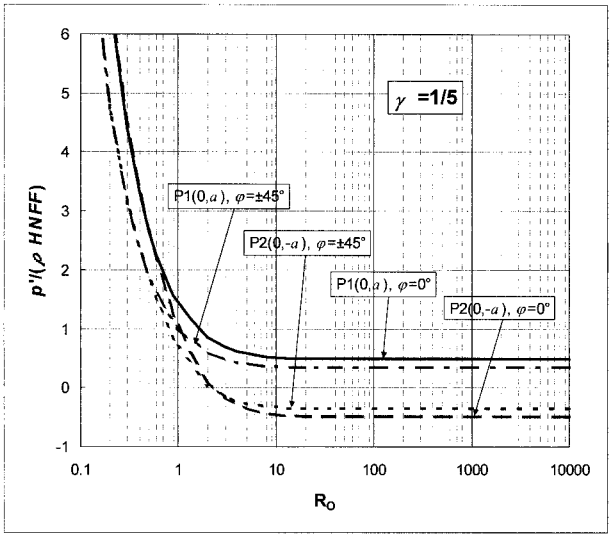

FIG. 6. The variations of the normalized pressure perturbation fields as a function of Ro at the points P1(0, a) and P2(0, $-a$), as indicated in Fig. 1, around an elliptical horizontal cross-sectional barriers ($\gamma = 1/5$), as induced by uniform airflows having incoming DI $\varphi = 0°$ and $\varphi = \pm 45°$, as indicated by the labels.

are in accordance with the results obtained for the circular hill simulation.

In the absence of the Coriolis effect (Ro = ∞), the pressure perturbation fields obtained with complementary DI ($\varphi \leftrightarrow -\varphi$) are symmetric with respect to both mountain axes of symmetry. But when the Coriolis effect is introduced (Ro = 1 and 0.5), this symmetry is broken. As seen in Fig. 5 for $\varphi = \pm 45°$, although $Cp(0, \pm a)|_{\varphi}$ remains equal to $Cp(0, \pm a)|_{-\varphi}$, the pressure perturbation fields are just the mirror images with respect to the Y axis. The departure of the incoming flow from pure normal ($\varphi \neq 0$) is followed by a reduction of the absolute values of the pressure perturbation (Figs. 5 and 6). Detailed calculations for different DI show that the larger the DI, the smaller the pressure perturbation values. This is a consequence of the fact that the blocking effect of the mountain decreases with its effective cross section. The last statement holds only for $\gamma < 1$. For $\gamma = 1$, the pressure perturbation is independent of the DI, while for $\gamma > 1$, it increases when the DI increases.

2) WIND PERTURBATION FIELDS

The surface total wind velocity field around the elliptical barrier demonstrated in Fig. 7 conserves the general features of the circular case. For Ro = ∞ and $\varphi = 0°$, the incoming flow splits into two horizontal symmetrical branches in a stagnation point, located upstream, on the normal axis ($x = 0$). The upstream blocking effect generates the same total winds on both sides. For Ro = ∞ and $\varphi = \pm 45°$, the deflection of the flow is no longer symmetric, but due to the absence of the Coriolis effect, the wind velocity fields are mirror images with respect to the Y axis. The differences between the flow patterns for $\varphi = +45°$ and $\varphi = -45°$ should not be attributed to the perturbation fields, which are identical for both DIs, as can be seen in Fig. 8a. The different wind patterns result from the superposition of the perturbation fields and the incoming flow, which subjected to the sign convention adopted above.

When the Coriolis effect is introduced (Ro = 1 and $\varphi = 0°$), the surface wind velocity field shows an asymmetric lateral deflection with stronger winds on the left than on the right side of the mountain (Fig. 7b). On the left side of Fig. 8b, the normal component contributes to increase the wind behind the barrier regardless of whether the parallel component increases the wind velocity in front of the barrier. For $\varphi = \pm 45°$, the superposition of the flow perturbation and the incoming flow gives different flow patterns around the barrier. The wind perturbation is stronger for $\varphi = +45°$ than for $\varphi = -45°$. The absolute values of both components, for both DIs, are larger on the left than on the right edge. Near the mountain, the distributions of the normal component of the wind perturbation look similar regardless of whether the parallel component values differ considerably in front of the mountain (the values are higher for positive than for negative DI). When the incoming wind is added to the perturbation field, the total wind intensity is reduced in front of the barrier for $\varphi = +45°$ and enhanced for $\varphi = -45°$. The difference between the total wind speed on both flanks of the mountain is larger for $\varphi = -45°$ than for $\varphi = +45°$, for the set of values used in the present simulations. When the Rossby number decreases to 0.5, no significant changes on the wind perturbation and the total wind fields can be mentioned, except that the wind perturbation field shows a tendency to shrink around the mountain (Figs. 7c and 8c).

The linear model was used to calculate the normalized total wind on the right ($-b$, 0, 0) and left (b, 0, 0) sides of the elliptical mountain, and the results versus Ro, for the three DIs used in the simulations, are presented in Fig. 9. These particular points were chosen because they are relevant to the comparison of the calculated values to the experimental data collected during PYREX at the edges of the Pyrénées (Bénech et al. 1998).

For values of Ro greater than 20, the normalized total winds at the edges converge to asymptotic values that are determined by the DI. The value of Ro = 20 can be accepted as a criterion for the appearance of the Coriolis effect as a factor influencing the flow for this shape of mountain. Under these conditions and for normal incidence ($\varphi = 0°$), the wind at the edges is found to be 20% faster than the normal component of the incoming flow ($V = 10$ m s^{-1}). The intensity of the wind exceeds V by 90% at the left edge for $\varphi = -45°$ and, by symmetry, at the right side for $\varphi = +45°$. The convergence of the normalized slower velocities in the

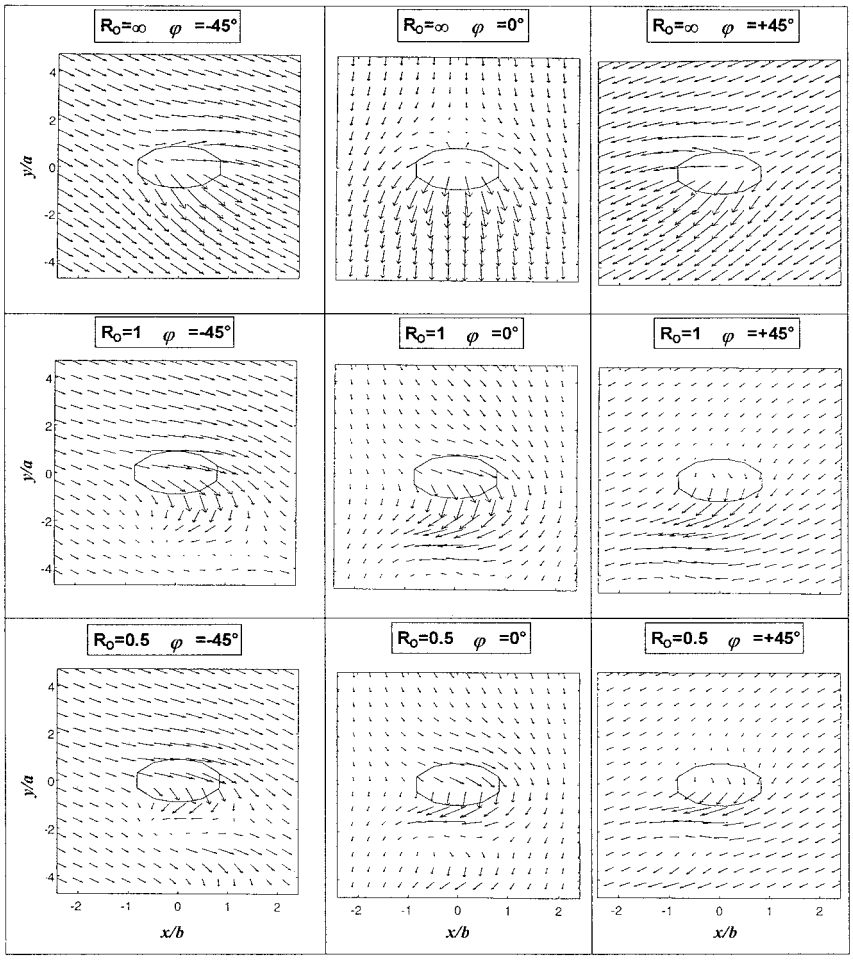

FIG. 7. As in Fig. 5 except for the ground level, total wind vector field.

opposing edges that correspond to $\varphi = 0°$ is only a fortuitous result of the combination of the shape of the mountain and the incoming velocity used in this specific experiment.

For Ro smaller than 20, the flow is dramatically modified by the Coriolis effect in different ways at each edge of the mountain. On the left side, the normalized total wind reaches a maximum value for all the DIs ($-45°$, $0°$, and $+45$) at different values of Ro (1.8, 1.3, and 0.4, respectively), indicating that the flow regime on the left edge changes when the Coriolis effect is considerable. While the dependence of these maximum positions on the DI seems to be linear in the range examined here, a rigorous study of this statement is beyond the scope of this paper. On the right side, the normalized wind oscillates with a general tendency to decrease slowly for all the DIs. For $\varphi = +45°$, the highest normalized wind velocity on the left side is attained at small values of Ro, while on the right at Ro > 5.

A measure of the asymmetry of the flow previously discussed is the difference between the normalized total wind velocities at the left and right mountain flanks, demonstrated in Fig. 10 as a function of Rossby number, for the three DIs. In Fig. 10, it is observed that for Ro > 20, the difference of normalized wind velocities for $\varphi = -45°$ converges asymptotically to the positive value 0.5, implying that, due to the effect of the DI, the wind on the left is stronger than on the right side by $0.5V$. For $\varphi = +45°$, the difference converges to the complementary negative value -0.5, implying that in this case the wind on the right is stronger than on the left side by $0.5V$. This correlation of the flow characteristic in the absence of the Coriolis effect is expected in view of the symmetry around normal incidence ($\varphi = 0°$). But when the Coriolis effect becomes important (Ro < 20), the symmetry is disrupted and the wind differences are no longer complementary. For northwesterly flows ($\varphi = -45°$), the model predicts that the wind velocity in the left branch (east side) will be always stronger than on the right branch (west side). This asymmetry will be maximal for Ro $= 2$, attaching a value of $1.5V$, which implies that due to the combined contributions of DI

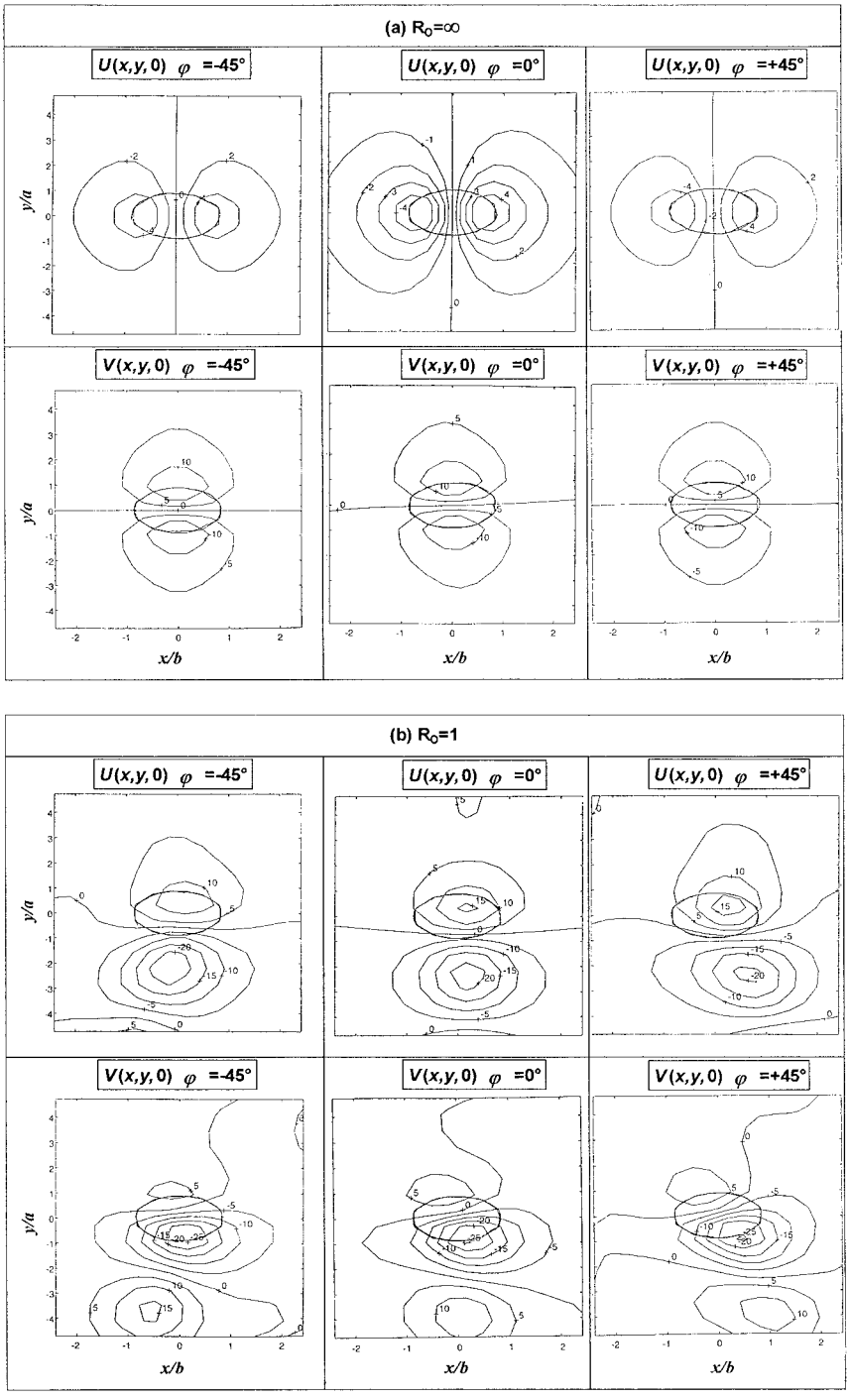

FIG. 8. The normalized total wind parallel (to the principal, *X* oriented, ellipse axis) *U* component (upper row) and normal *V* component (lower row) fields around an elliptical barrier ($\gamma = 1/5$), as induced by airflows having incoming DI $\varphi = -45°$ (left column), $\varphi = 0°$ (midcolumn) and $\varphi = +45°$ (right column), and Rossby numbers (a) Ro = ∞ (Coriolis effect absent), (b) Ro = 1, and (c) Ro = 0.5.

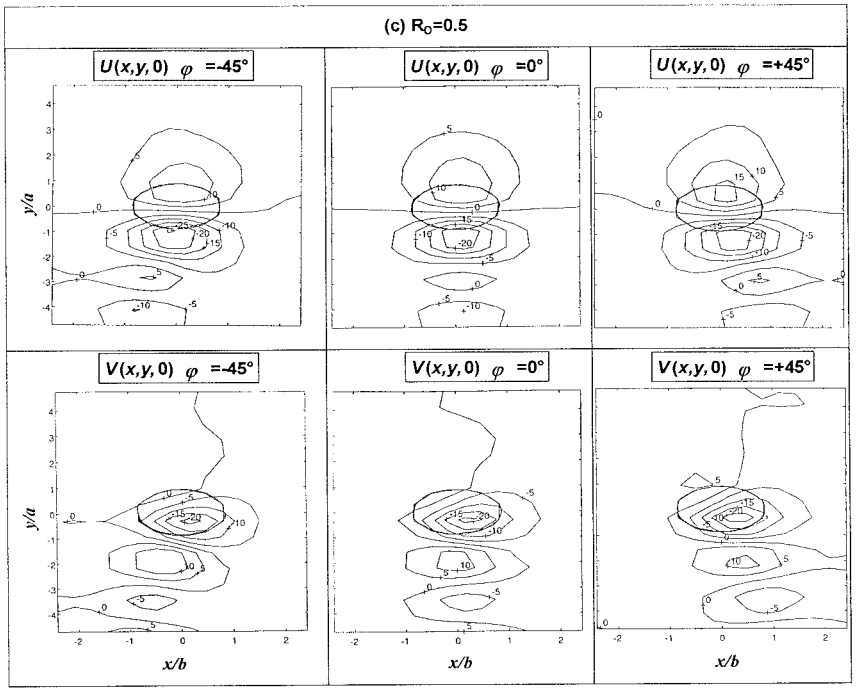

FIG. 8. (*Continued*)

and the Coriolis effect, the wind on the left is stronger than on the right side by 1.5*V*. The partition of the contributions to the asymmetry is one-third by DI and two-thirds by rotational effect. This partition depends not only on Ro, as demonstrated by the curve for $\varphi = -45°$, but also on DI, as is deduced by comparing the different shapes of the curves for $\varphi = -45°$ and $\varphi = 0°$. The latter represents the pure rotational effect at normal incidence. For southwesterly flows ($\varphi = +45°$), the model predicts that for a partial range of Rossby numbers (Ro < 10) the wind will be stronger in the left (west side) than in the right (east side) branch, while for the remaining values of Ro, the mode will be inverted.

Recalling that $\varphi = -45°$ represents northwesterly flows and $\varphi = +45°$ southwesterly flows, it can be concluded that the linear model predicts a substantially different flow asymmetry for both flow categories and for Rossby numbers in the range 0.3 to 20. In general, for almost all the variation range of Ro, the asymmetry

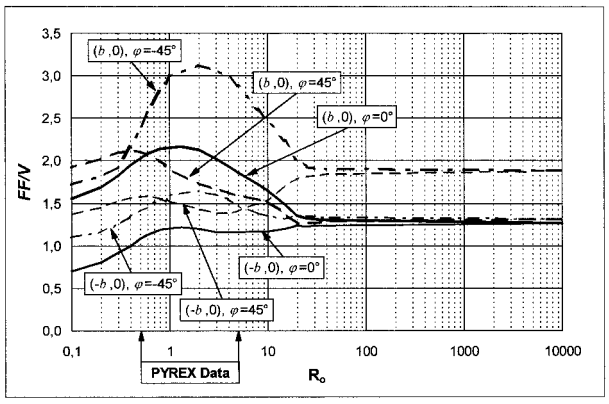

FIG. 9. The dependence on the Rossby number of the normalized total wind at ground level, induced on flanks (b, 0) and ($-b$, 0) of an elliptical ($\gamma = 1/5$) barrier (Fig. 1) by uniform airflows having DI $\varphi = 0°$, $\varphi = +45°$, and $\varphi = -45°$, as indicated by the harrowed labels. The harrowed gray label indicates the range of Rossby numbers observed in the PYREX experiment.

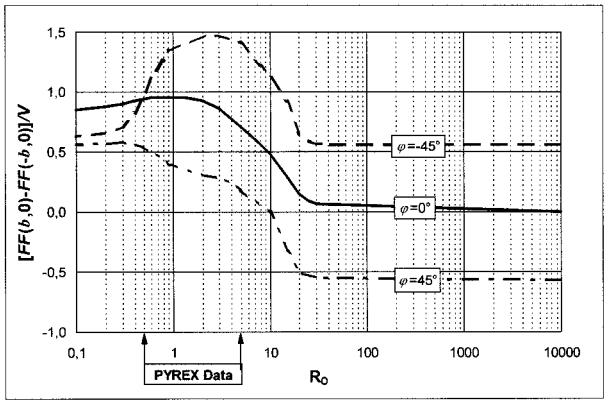

FIG. 10. The dependence on the Rossby number of the difference between the normalized, ground level, total wind velocities at the flanks P1(0, a) and P2(0, $-a$) of an elliptical ($\gamma = 1/5$) barrier, as induced by uniform airflows having DI $\varphi = 0°$, $\varphi = +45°$, and $\varphi = -45°$, as indicated by the labels. The harrowed gray label indicates the range of Rossby numbers observed in the PYREX experiment.

is considerably more pronounced in northerly than in southerly flows. These results are in agreement with the experimental evidences collected during PYREX. Northwesterly synoptic winds originate on the eastern side of the Pyrénées; tramontane winds are much stronger than cierzo winds, blowing at the same time on the western side (Bénech et al. 1998; their Figs. 13a, 13b, and 14a). By contrast, during southwesterly synoptic flows, bochorno winds blow in the west side at almost the same velocities as marin-autan winds on the east side of the Pyrénées (Bénech et al. 1998; their Figs. 13c, 13d, and 14b).

The validity of the feature of the flow described here will be tested in section 4 with regard to the field measurements carried out during the PYREX experiment.

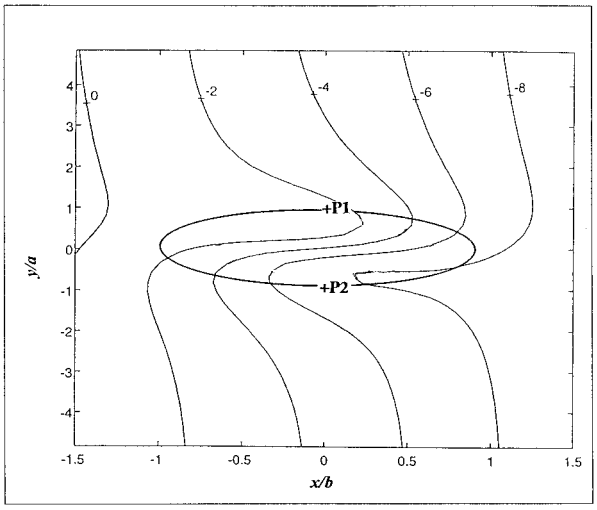

FIG. 11. The deformation of the pressure field (hPa, relative to the leftmost isobars), simulated using the numerical algorithm that implements the solution of the linear model for the conditions at 0600 UTC 16 November 1990 (IOP9) with Fr = 0.381 and Ro = 4. The incoming air mass approaches the barrier from the upper part of the figure at nearly normal incidence (Bénech et al. 1998; Table 1a).

4. Application to PYREX IOPs

a. Methodology

The PYREX experimental setup and operational procedure that are relevant to the present analysis are described in detail in Bénech et al. (1998). During the 10 IOPs, 6-h-interval radiosoundings were carried out at Toulouse or Zaragoza to characterize the northerly and southerly flows, respectively. The measured profiles were linearized, and the parameters required for the characterization of the incoming flow were determined at 3000 m MSL altitude. Those parameters are total wind velocity FF, wind direction of incidence φ, and potential temperature θ. The values of the basic parameters and the parameters that are input to the linear model to specify the incoming flow characteristics are given in Bénech et al. (1998; their Table 1). To be consistent with the linear theory foundation it is assumed that the properties of the incoming air masses are sufficiently well defined by the input set required to start the linear model, and therefore the following analysis will be constrained to this limited set of variables. This assumption implies that, at the scale of the Pyrénées range, the mean synoptic wind and the mean stability are representative of the meteorological conditions and that the synoptic pressure gradient, which drives the incoming flow, is nearly homogeneous. It is understood that those assumptions may become a source of dispersion of the data analyzed. Another source of data scatter may be the presence of important mountain chains adjacent to the Pyrénées (Bénech et al. 1998), which are idealized in the simulations by an isolated elliptical mountain.

b. Comparison of simulated and measured surface pressure fields

The simulated surface total pressure field is the superposition of the synoptic component and the pressure perturbation p', which is calculated by using the linear model. Since the synoptic wind is assumed to be geostrophic, its components can be calculated using the following equations:

$$\frac{\partial p}{\partial y} = -U\rho f \tag{12}$$

and

$$\frac{\partial p}{\partial x} = V\rho f. \tag{13}$$

Each parameter set measured during PYREX IOPs (Bénech et al. 1998; their Table 1) was used to start up the linear model simulations of the airflow around the Pyrénées, idealized by the 3D elliptical mountain described above (Fig. 2). The pressure perturbation field calculated for the conditions at 0600 UTC 16 November 1990 (IOP9), with Fr = 0.381 and Ro = 4, is shown in Fig. 11. The isobars are deformed by the mountain, with relative high pressure windward and low pressure leeward of the barrier. The pressure dipole intensity, measured by the difference between the pressure at the points P1(0, a) and P2(0, $-a$), is approximately 6 hPa (Fig. 11). The surface pressure deduced from the PERIDOT analysis conducted on 16 November 1990 (Bénech et al. 1998; their Fig. 8a) indicates the same morphology and a pressure dipole intensity of about 8 hPa. In general, the analysis shows a good morphological fit of the results of the linear model simulations to the experimental pressure fields, although some differences between the pressure dipole intensities have to be mentioned.

A quantitative comparison of the simulated and ex-

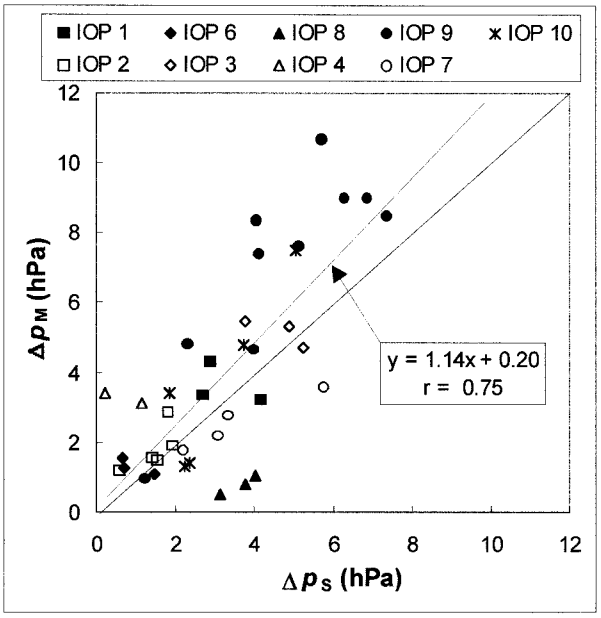

FIG. 12. The pressure dipole intensities deduced from experimental data (index M) vs the corresponding simulated values (index S). The IOPs of northerly and southerly flow categories are indicated by filled and empty symbols, respectively. The regression line for all the points (solid line), its equation, and the correlation coefficient are also indicated.

perimental pressure fields is performed through the difference between the pressure at P1(0, a) and P2(0, $-a$). The simulated pressure dipole intensities were evaluated for all PYREX events (one symbol by IOP), as described in Bénech et al. (1998; their Table 1). The experimental pressure dipole intensities were evaluated using the measurements at Pau, located on the north side near point P1, and Huesca, located on the south side near point P2 (Bénech et al. 1998; their Fig. 1a). Figure 12 shows the measured versus the simulated pressure dipole intensities. The regression line for all the points, having a slope close to 1 (1.14) with almost no bias (0.2) and a good correlation coefficient (0.75), indicates a general agreement of the values predicted by the linear theory and the experimental data. Somewhere, the linear model slightly underestimates the pressure dipole intensity, especially for northerly synoptic flows. The remarkable exceptions are the points corresponding to IOP8, for which the measured dipoles are extremely low when compared with the model predictions and also with the pressure drag measurements (Bénech et al. 1998; their Table 1a), which are close to the total average. This anomaly may be attributed to experimental errors originated in instrumental malfunction. Apart from nonlinear dynamic effects, which are not accounted for by the linear theory, thermal and friction effects due to ground roughness (Reisner and Smolarkiewicz 1994) may also contribute to the scattering of the points. Thermal effects in the vicinity of the Pyrénées were estimated to contribute from 30% to 85% of the total pressure drag (Bessemoulin et al. 1993). Since this thermally induced contribution to the pressure drag is not accounted for in the present study, considerable differences can be expected between the measured and simulated pressure dipole values, especially when low drag values are present. However, in the next section it will be shown that the regional winds generated on the lateral sides of the Pyrénées are well matched by the linear theory alone.

c. *Comparison of simulated and measured regional wind intensities on the edges of the Pyrénées*

To assess the capability of the linear theory to predict the deflected winds around a major mountain range, the simulated winds on the lateral sides of the elliptical mountain, at the locations (b, 0) and ($-b$, 0), will be compared to the wind data measured during PYREX IOPs at 100 to 500 m AGL in Pamplona and Port la Nouvelle/Cap Creus, located near the western and eastern edges of the Pyrénées, respectively. The same comparison is made also with the wind data measured in Zaragoza located inside the Ebro valley and greatly affected by the airflow deviated on the west side.

The comparison of the calculated and experimental values shows total compatibility regarding the asymmetry of the flow, when it is categorized by northerly and southerly incoming directions. The asymmetry of the wind velocity fields documented during PYREX is extensively discussed in Bénech et al. (1998); it is a key point in the applicability of the linear theory to describe blocked flows. This asymmetry is strong for northerly flows and weak for southerly flows (Bénech et al. 1998; their Fig. 14). For Ro values ranging between 0.5 and 5, the linear model result, shown in Fig. 10, depicts the same asymmetry features. For $\varphi = -45°$ (northwesterly category), the total wind difference is large and decreases when the DI turns to positive values (southwesterly category).

1) NORTHERLY SYNOPTIC FLOW CATEGORY

Two names are associated to the regional winds in the present category: the tramontane wind that blows on the east side and the cierzo that blows on the west side of the Pyrénées.

The normalized tramontane wind intensities (FF/V), deduced from the experimental data at 500 m AGL (maximum wind intensity), are plotted against the corresponding simulated values in Fig. 13a. The simulated tramontane wind intensities for Ro $\geq$ 2 (which corresponds to Fr $\geq$ 0.2) are in fair agreement with the experimental data. When Ro $<$ 2 (Fr $<$ 0.2), the simulated values are greater than the measured.

For the cierzo wind, the first comparison is made with

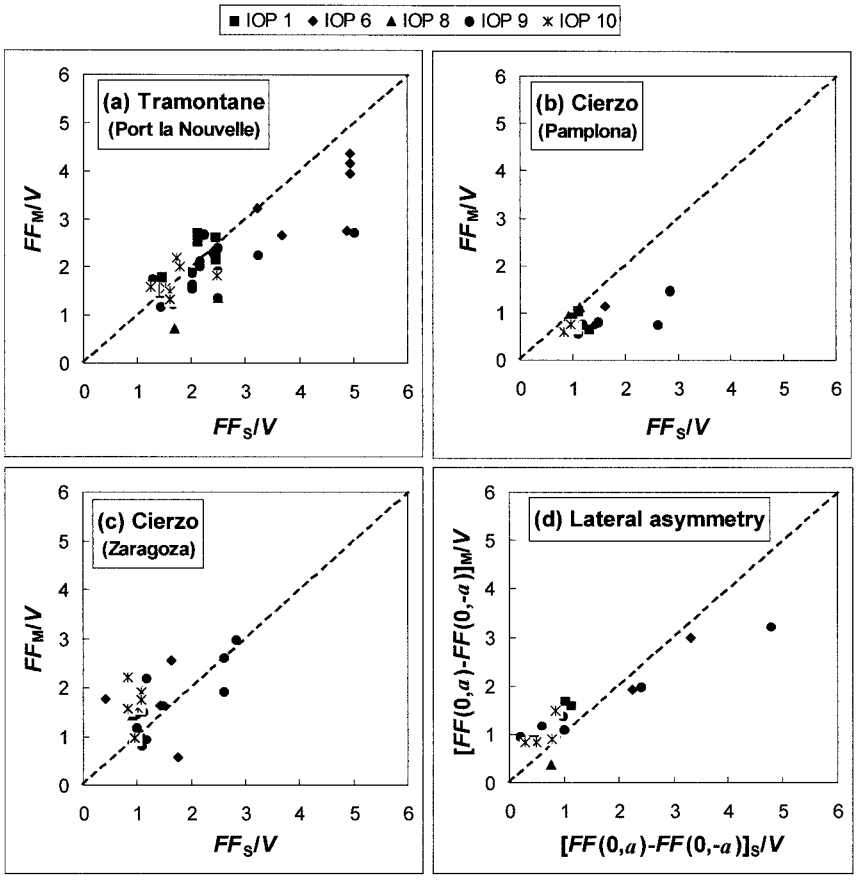

FIG. 13. The normalized wind velocity at 500 m AGL deduced from experimental data (index M) vs the corresponding simulated values (index S), when northerly flows induced: (a) tramontane and (b) and (c) cierzo winds, for soundings carried out at Port la Nouvelle, Pamplona, and Zaragoza, respectively. The differences between the values measured at the edges of the Pyrénées vs the differences between the values calculated for the conditions specified above are plotted in (d). Each IOP is represented by a different symbol.

the experimental data obtained from the soundings made in Pamplona, located at 400 m MSL and probably subjected to local dynamic processes. As seen in Fig. 13b, the values are weaker than on the east side, as predicted by the linear theory. However, the experimental wind intensities are, in general, slightly weaker than the simulated values.

The second comparison is made with the values deduced from measurements at Zaragoza, located in the Ebro valley. The experimental data follow the same trend predicted by the linear model (Fig. 13c). However, the measured wind intensities are somewhat greater than the calculated values, probably due to the channeling effect of the Ebro valley. When comparing Fig. 13a with Fig. 13c, it can be seen that tramontane winds are, on the average, stronger than Cierzo winds.

The differences between the wind intensities on the lateral sides of the Pyrénées are compared in Fig. 13d. For high Rossby numbers (Ro $\geq$ 2), the experimental wind differences are slightly greater than the linear prediction, while for Ro $<$ 2, the opposite holds. The simulated wind differences agree fairly well with the experimental values, showing that the lateral asymmetry of the flow is well explained by the linear theory, for the northerly flow category. Moreover, the asymmetric flow on the lateral edges of the Pyrénées is closely coupled to the Coriolis effect and the DI of the incoming flow.

2) SOUTHERLY SYNOPTIC FLOW CATEGORY

The regional wind names associated with this categories are, on the west side, the bochorno moderate winds that climb up the Ebro valley, and on the east side, the marin wind, which farther upstream becomes the autan wind.

In spite of the fact that the statistical study in Bénech et al. (1998) showed that the southerly synoptic flows documented during PYREX are weakly correlated to the pressure perturbation field, the linear model was

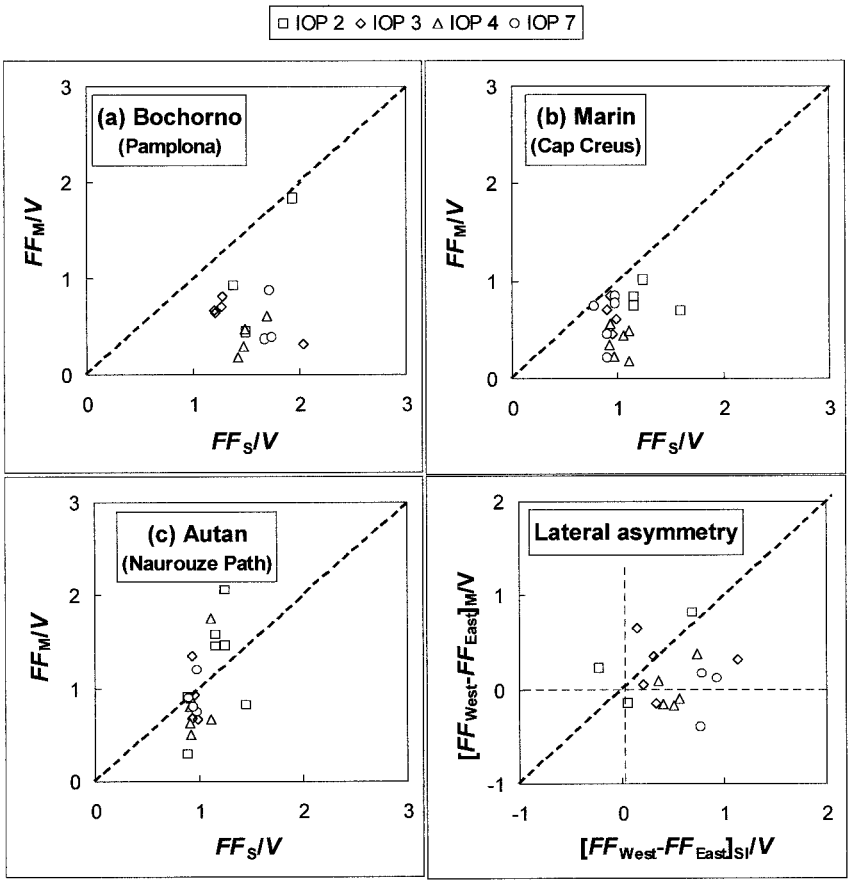

FIG. 14. As in Fig. 13, when southerly flows induced: (a) bochorno, (b) marin, and (c) autan winds for soundings carried out at Pamplona, Cap Creus, and Naurouze Path, respectively.

nevertheless applied, using the data collected at Zaragoza.

Bochorno wind intensities at 500 m AGL were measured at Pamplona. The values predicted by the linear model are greater than the experimental, as can be seen in Fig. 14a. Contrary to the linear theory prediction that the wind intensity on the left side should always be greater than the normal component V of the incoming flow, the measured values are, in general, weaker than calculated. The most likely explanation of this discrepancy is that southerly flows are strongly disturbed on the west side of the Pyrénées by adjacent topographic obstacles (e.g., Iberic chain, Cantabric chain, Ebro valley) before they reach the main barrier.

Marin wind intensities, deduced from the soundings at Cap Creus, are in good agreement with the linear theory predictions (Fig. 14b); they are relatively weak as expected from the retardation effect due to the Coriolis component. The linear model applied to the autan winds sounded at the Naurouze Path also gave satisfactory results (Fig. 14c). Since the flow asymmetry is not clearly related to the Rossby number, it can be inferred that the difference between the wind intensities on the flanks of Pyrénées at 500 m AGL is insensitive to the Rossby number variations for southerly flows (Fig. 14d).

5. Summary and conclusions

A three-dimensional model based on the linear theory was briefly described. The model can deal with uniform, stable airflows over families of 3D elliptical or Gaussian mountains. Gaussian mountains were not consider in the present work because the Pyrénées range was best fitted by the elliptical cross section. The model incorporates the earth rotation (Coriolis effect) and is not limited to normal incidence to the mountain principal axis. The pressure and horizontal wind perturbation fields are expressed in terms of double Fourier integrals.

Numerical simulations of airflow patterns were carried out using an algorithm that implements the linear model to evaluate the sensibility of mesoscale blocked

airflows to the Coriolis effect and upwind DI variations. Two elliptical topographic barriers were analyzed: a circular cross-section mountain with an aspect ratio of unity and a mountain with an aspect ratio 0.2 that matches the Pyrénées range. The normal (to the principal axis of the mountain) component of the incoming stable airmass wind velocity was kept constant at value 10 m s^{-1}, and its Froude number was kept constant at value 0.33. Thus, the variations of the Coriolis effect were implicitly represented by the Rossby number, varying from 0.1 to 10000 ($\sim\infty$). Considering the symmetry properties of the mountains, the three flow categories defined according to the DIs of 0°, −45°, and +45° are normally incident northerly and southerly flows, northwesterly and southeasterly flows, northeasterly and southwesterly flows, respectively.

For normal incident incoming flows, in the absence of the Coriolis effect (large Rossby numbers), the airflow is split into two symmetrical branches at a stagnation point located on the normal axis in front of the mountain. For Rossby numbers smaller than 20, the linear model predicts substantial flow asymmetry, with stronger winds in the left rather than in the right branch. Thus, the Rossby number of 20 can be accepted as a critical value for the Coriolis effect to become significant. This asymmetry can be enhanced or counterbalanced by the synoptic-driven wind, depending on its DI. For northwesterly flows, the model predicts that the wind velocity in the left branch (east side) will always be stronger than in the right branch (west side). For southwesterly flows, the model predicts that, for a partial range of Rossby numbers smaller than 10, the wind will be stronger in the left (west side) than in the right (east side) branch, while for the remaining values of Ro, the situation will be inverted. In general, while the Coriolis effect triggers the flow asymmetry, the DI can enhance or inhibit it. Consequently, for almost all of the variation range of Ro, the asymmetry is considerably more pronounced in northerly than in southerly flows.

The results of numerical simulations applied to parameter sets resembling the airflows documented during the PYREX experiment show that the intensity of deflected winds induced by the blocking effect of a mesoscale mountain such as the Pyrénées can be explained through the linear theory. The linear theory explains well the asymmetry of the deflected winds between northerly flows (tramontane–cierzo) and southerly flows (marin–bochorno) by the combined effect of the DI of the incident airflow and the Coriolis force.

A preliminary qualitative validation is found in the fact that during northerly synoptic flows, the tramontane winds observed on the eastern flank of the Pyrénées were considerably stronger than cierzo winds in the eastern edge. During southerly flows, on the contrary, bochorno (west side) and marin-autan (east side) winds were found to blow at almost the same velocities.

Quantitative comparisons show that the simulated tramontane wind intensities for Rossby numbers greater than 2 are in fair agreement with the experimental data, while for Rossby numbers smaller than 2, the calculated values are greater than the measured. For cierzo winds, the measured velocities are, in general, slightly weaker than the simulated values. The simulated wind differences agree fairly well with the experimental values, showing that the lateral asymmetry of the flow is well explained by the linear theory for the northerly flow category. The values predicted by the linear model are greater than the velocities of bochorno winds, perhaps because southerly flows are strongly disturbed on the west side of the Pyrénées by adjacent topographic obstacles (e.g., Iberic chain. Cantabric chain, Ebro valley) before they reach the main barrier, marin winds intensities are in good agreement with the linear theory predictions, being relatively weak as expected from the retardation effect of the Coriolis component. Due to the low intensity of the southerly winds, a quantitative estimation of the linear model applicability is less explicit than for the northerly category, but as pointed out previously, the general trend is in agreement with experimental values. The linear theory also shows that the wind intensities are directly linked with the mountain waves.

The linear theory formulation is relatively simple and its numerical implementation affordable even with reduced resources. It may be rigorously argued that it cannot be applied to blocked flows with low Froude numbers. But the extrapolations presented here were sufficient to describe, explain, and quantify many of the flow characteristics around the Pyrénées. This is in accordance with recent 3D nonlinear numerical simulations (Ólafsson and Bougeault 1996, 1997) that show that when rotational and frictional effects are accounted for in the model, some of the results converge to the predictions of the linear theory.

Further applications of the linear model presented here should be carefully managed in consideration of the assumptions made in its development. The uniformity and thermal stability of the flow are basic conditions, and the results may be inadequate for extremely low Froude numbers when nonlinear effects become dominant. Nevertheless, when applied in the correct spatial domain, extrapolated over the correct range of Froude and Rossby numbers, and properly assessed by experimental evidences, as was the case in the present work, the linear theory remains a relatively simple method with the capability to describe blocked flows in front and in the flanks of the topographic barrier.

Acknowledgments. The PYREX experiment was made possible by the participation of a large number

of institutes and funding agencies. The participating institutes are CNRM, CRPE, LA, LAMP, LMD, LSEET, SA, EDF for France; INM, UV, UIB for Spain; and DLR for Germany. Funding was provided by Météo-France, INM, INSU (ARAT, PATOM and PAMOY programs), CNES, EDF, DLR, and Région Midi-Pyrénées. Much technical help was provided by CEV, ENM, and the French and Spanish Air Force and air control authorities. We would like to express our gratitude to J. C. André, D. Cadet, D. Guedalia, and A. Ascaso Liria for their help in the planning of this program. We also would like to express our deep appreciation to the many colleagues who have participated to the success of the experiment through enormous personal commitment.

APPENDIX

Solution of Linearized System

After some algebra, the system of Eqs. (4)–(7) in the text can be reduced into the single equation in terms of w':

$$\frac{\partial^2 A}{\partial z^2} + \delta B + C = 0, \tag{A1}$$

where

$$A = \frac{U^2}{V^2}\frac{\partial^2 w'}{\partial x^2} + \frac{\partial^2 w'}{\partial y^2} + \frac{2U}{V}\frac{\partial^2 w'}{\partial x \partial y} + \frac{f^2}{V^2}w', \tag{A2}$$

$$B = \frac{U^2}{V^2}\frac{\partial^2}{\partial x^2}(\nabla_h^2 w') + \frac{\partial^2}{\partial y^2}(\nabla_h^2 w') + \frac{2U}{V}\frac{\partial^2}{\partial x \partial y}(\nabla_h^2 w'), \tag{A3}$$

$$C = \frac{N^2}{V^2}(\nabla_h w'), \tag{A4}$$

and

$$N = \sqrt{\frac{g}{\theta_h}\frac{d\theta}{dz}}, \tag{A5}$$

where N is the Brunt–Väisälä frequency, θ_h is the potential temperature, and $d\theta/dz$ is the potential temperature gradient. For a stationary steady flow, w' can be written using double Fourier transform integrals:

$$w'(x, y, z) = \int_{-\infty}^{\infty}\int_{-\infty}^{\infty} \tilde{w}(k, l, z) e^{i(kx+ly+mz)}\, dk\, dl, \tag{A6}$$

where k, l, and m are the lateral, normal, and vertical wave numbers, respectively. Here, $\tilde{w}$ is the inverse Fourier transform of w'. The vertical wavenumber m depends on k and l through the equation, deduced from Eq. (A1):

$$m^2 = \left[\frac{k^2 + l^2}{(Uk + Vl)^2 - f^2}\right][N^2 - \delta(Uk + Vl)^2]. \tag{A7}$$

The values of p', u', and v' are found by solving the following double Fourier integrals:

$$p'(x, y, z) = \int_{-\infty}^{\infty}\int_{-\infty}^{\infty} \tilde{p} e^{im(k,l)z} e^{i(kx+ly)}\, dk\, dl, \tag{A8}$$

$$u'(x, y, z) = \int_{-\infty}^{\infty}\int_{-\infty}^{\infty} \tilde{u} e^{im(k,l)z} e^{i(kx+ly)}\, dk\, dl, \tag{A9}$$

and

$$v'(x, y, z) = \int_{-\infty}^{\infty}\int_{-\infty}^{\infty} \tilde{v} e^{im(k,l)z} e^{i(kx+ly)}\, dk\, dl, \tag{A10}$$

where $\tilde{p}$, $\tilde{u}$, and $\tilde{v}$ are inverse Fourier transform of the pressure perturbations p' and of the horizontal wind velocity deviations u' and v', given by

$$\tilde{p} = i\rho\left[\frac{N^2}{m}\right]\tilde{\eta} \tag{A11}$$

$$\tilde{u} = -i\frac{N^2}{mV}\left\{\frac{[kl + (U/V)k^2] + i(fl/V)}{[l + (U/V)k]^2 - (f^2/V^2)}\right\}\tilde{\eta} \tag{A12}$$

$$\tilde{v} = -i\frac{N^2}{mV}\left\{\frac{[l^2 + (U/V)kl] - i(fk/V)}{[l + (U/V)k]^2 - (f^2/V^2)}\right\}\tilde{\eta}, \tag{A13}$$

where $\tilde{\eta}$ is the inverse Fourier transform of the function $\eta(x, y, z)$, which is used to represent the vertical displacement of the fluid parcel or the density surface.

The kinematics condition for a steady flow in the lower boundary states

$$w' = \frac{d\eta}{dt} \approx U\frac{\partial \eta}{\partial x} + V\frac{\partial \eta}{\partial y} \tag{A14}$$

and the lower boundary condition is imposed by the terrain shape

$$\eta(x, y, 0) = h(x, y), \tag{A15}$$

where $h(x, y)$ characterizes the surface topography, as defined in Eq. (2). From Eq. (A15), it follows that

$$\tilde{\eta}(k, l, 0) = \tilde{h}(k, l), \tag{A16}$$

where $\tilde{h}(k, l)$ represent the inverse Fourier transform of the mountain shape and is given by

$$\tilde{h}(k, l) = \frac{1}{4\pi^2}\int_{-\infty}^{\infty}\int_{-\infty}^{\infty} h(x, y) e^{-i(kx+ly)}\, dx\, dy. \tag{A17}$$

The analytical expressions for the perturbation fields of the surface pressure p' and surface wind velocities u' and v', over the 3D elliptical mountains defined by Eq. (2), are conveniently expressed in horizontal polar coordinates (r, ϕ):

$$\left.\begin{aligned} kb &= r\cos\phi, \\ la &= r\sin\phi, \\ r &= [(kb)^2 + (la)^2]^{1/2}, \end{aligned}\right\} \tag{A18}$$

which are attached to the orthogonal system described in Fig. 1 by the equations

$$\left.\begin{aligned} X &= x/b = R\cos\theta, \\ Y &= y/a = R\sin\theta, \\ R &= (X^2 + Y^2)^{1/2}. \end{aligned}\right\} \tag{A19}$$

For normal incidence, $U = 0$ and the perturbation fields are

$$p'(X, Y) = \rho HNV\,\mathrm{Re}\left\{ i \int_0^{\pi} \int_0^{\infty} \frac{[\cos^2\phi - (fa/V)r^{-2}]^{1/2}}{[\cos^2\phi + (a/b)^2\sin^2\phi]^{1/2}} \left[1 - \left(\frac{V}{Na}\right)^2 r^2\cos^2\phi \right]^{1/2} G(r, \phi)\, dr\, d\phi \right\}, \tag{A20}$$

$$u'(X, Y) = -HN\,\mathrm{Re}\left\{ i \int_0^{2\pi} \int_0^{\infty} \frac{[(a/b)\cos\phi\sin\phi - ir^{-1}(fa/V)\cos\phi]}{[\cos^2\phi + (a/b)^2\sin^2\phi]^{1/2}} \frac{[1 - (V/Na)^2 r^2\cos^2\phi]^{1/2}}{[\cos^2\phi - (V/Na)^2 r^{-2}]^{1/2}} G(r, \phi)\, dr\, d\phi \right\}, \tag{A21}$$

and

$$\upsilon'(X, Y) = -HN\,\mathrm{Re}\left\{ i \int_0^{2\pi} \int_0^{\infty} \frac{[\cos^2\phi - ir^{-1}(fa/V)(a/b)\sin\phi]}{[\cos^2\phi + (a/b)^2\sin^2\phi]^{1/2}} \frac{[1 - (V/Na)^2 r^2\cos^2\phi]^{1/2}}{[\cos^2\phi - r^{-2}(fa/V)^2]^{1/2}} G(r, \phi)\, dr\, d\phi \right\}, \tag{A22}$$

where Re indicates the real part of the solutions and

$$G(r, \phi) = e^{irR\cos(\phi - \theta)} r\tilde{H}(r) \tag{A23}$$

with

$$\tilde{H}(r) = \frac{1}{2}\left(\frac{r}{2}\right)^{\mu-1} \frac{K_{\mu-1}(r)}{\Gamma(\mu)} \tag{A24}$$

for $\mu > 1/4$, where $K_{\mu-1}(r)$ is the Bessel function of imaginary argument and $\Gamma(\mu)$ is the gamma function. The dimensionless parameters used to characterize the dynamic incoming flow properties are Rossby and Froude numbers (Fr and Fa, relative to the top and the width of the mountain, respectively), aspect ratio of the mountain horizontal cross section (γ), and DI (φ) defined, respectively, by

$$\mathrm{Ro} = \frac{V}{fa}, \tag{A25}$$

$$\mathrm{Fr} = \frac{V}{NH} \quad \text{and} \quad \mathrm{Fa} = \frac{V}{Na}, \tag{A26}$$

$$\gamma = \frac{a}{b}, \tag{A27}$$

and

$$\varphi = \arctan\left(\frac{U}{V}\right). \tag{A28}$$

After Eqs. (A25)–(A27) are introduced into Eqs. (A20)–(A22), the solutions in terms of the dimensionless numbers are

$$p'(X, Y) = \rho HNV\,\mathrm{Re}\left\{ i \int_0^{\pi} \int_0^{\infty} \frac{[\cos^2\phi - \mathrm{Ro}^{-1}r^{-2}]^{1/2}}{[\cos^2\phi + \gamma^2\sin^2\phi]^{1/2}} [1 - \mathrm{Fa}^2 r^2\cos^2\phi]^{1/2} G(r, \phi)\, dr\, d\phi \right\} \tag{A29}$$

$$u'(X, Y) = -HN\,\mathrm{Re}\left\{ i \int_0^{2\pi} \int_0^{\infty} \frac{[\gamma\cos\phi\sin\phi - ir^{-1}\mathrm{Ro}^{-1}\cos\phi]}{[\cos^2\phi + \gamma^2\sin^2\phi]^{1/2}} \frac{[1 - \mathrm{Fa}^2 r^2\cos^2\phi]^{1/2}}{[\cos^2\phi - \mathrm{Fa}^2 r^{-2}]^{1/2}} G(r, \phi)\, dr\, d\phi \right\} \tag{A30}$$

$$\upsilon'(X, Y) = -HN\,\mathrm{Re}\left\{ i \int_0^{2\pi} \int_0^{\infty} \frac{[\cos^2\phi - ir^{-1}\gamma\mathrm{Ro}^{-1}\sin\phi]}{[\cos^2\phi + \gamma^2\sin^2\phi]^{1/2}} \frac{[1 - \mathrm{Fa}^2 r^2\cos^2\phi]^{1/2}}{[\cos^2\phi - r^{-2}\mathrm{Ro}^{-1}]^{1/2}} G(r, \phi)\, dr\, d\phi \right\}. \tag{A31}$$

REFERENCES

Beljaars, A. C. M., J. L. Walmsley, and P. A. Taylor, 1987: A mixed spectral finite-difference model for neutrally stratified boundary-layer flow over roughness changes and topography. *Bound.-Layer Meteor.,* **38,** 273–303.

Bénech, B., E. Koffi, A. Druilhet, P. Durand, P. Bessemoulin, J. Campins, A. Jansa, and B. Terliuc, 1998: Dynamic characteristics of regional flows around the Pyrénées in view of PYREX experiment data. Part I: Analysis of the pressure and wind fields and experimental assessment of the applicability of the linear theory. *J. Appl. Meteor.,* **37,** 32–52.

Bessemoulin, P., P. Bougeault, A. Genoves, A. Jansa, and D. Puech, 1993: Mountain pressure drag during PYREX. *Beitr. Phys. Atmos.,* **66,** 305–325.

Bougeault, P., B. Bret, P. Lacarrère, and J. Noilhan, 1991: An experiment with an advanced surface parameterization in a mesobeta-scale model. Part II: The 16 June simulation. *Mon. Wea. Rev.,* **119,** 2374–2392.

Buzzi, A., and S. Tibaldi, 1977: Inertial and frictional effects on rotating and stratified flow over topography. *Quart. J. Roy. Meteor. Soc.,* **103,** 135–150.

Drazin, P. G., 1961: On the steady flow of a fluid of variable density past an obstacle. *Tellus,* **13,** 239–251.

Hunt, J. R. C., S. Leibovich, and K. J. Richards, 1988: Turbulent shear flows over low hills. *Quart. J. Roy. Meteor. Soc.,* **114,** 1435–1470.

Imbard, M., A. Joly, and R. du Vachat, 1986: Le modèle de prévision numérique PERIDOT: Formulation dynamique et modes de fonctionnement. EERM Tech. Rep. 161, 36 pp. [Available from CNRM, 31057 Toulouse, France.]

Klemp, J. B., and D. K. Lilly, 1975: The dynamics of wave-induced downslope winds. *J. Atmos. Sci.,* **32,** 320–339.

——, and ——, 1978: Numerical simulation of hydrostatic mountain waves. *J. Atmos. Sci.,* **35,** 78–107.

Koffi, E., 1994: Caractérisation expérimentale de l'écoulement atmosphérique autour d'un massif montagneux (Expérience PYREX). Thése de doctorat 1764, Université Paul Sabatier, Toulouse, France, 258 pp. [Available from CRA, 65300 Lannemezan, France.]

Lyra, G., 1943: Theorie der stationären Leewellenströmung in freier Atmosphäre. *Z. Ang. Math. Mech.,* **23,** 1–28.

Mason, P. J., and J. C. King, 1985: Measurements and predictions of flow and turbulence over an isolated hill of moderate slope. *Quart. J. Roy. Meteor. Soc.,* **111,** 617–640.

Ólafsson, H., and P. Bougeault, 1996: No linear flow past an elliptic mountain ridge. *J. Atmos. Sci.,* **53,** 2465–2489.

——, and ——, 1997: The effect of rotation and surface friction on orographic drag. *J. Atmos. Sci.,* **54,** 193–210.

Phillips, D. S., 1984: Analytical surface pressure and drag for linear hydrostatic flow over three-dimensional elliptical mountains. *J. Atmos. Sci.,* **41,** 1073–1084.

Pierrehumbert, R. T., and B. Wyman, 1985: Upstream effects of mesoscale mountains. *J. Atmos. Sci.,* **42,** 977–1003.

Queney, P., 1948: The problem of airflow over mountains: A summary of theoretical studies. *Bull. Amer. Meteor. Soc.,* **29,** 16–26.

Reisner, M. J., and P. K. Somolarkiewicz, 1994: Thermally forced low Froude number flow past three-dimensional obstacles. *J. Atmos. Sci.,* **51,** 117–133.

Smith, R. B., 1979: The influence of the heart's rotation on mountain wave drag. *J. Atmos. Sci.,* **36,** 177–180.

——, 1980: Linear theory of stratified flow past an isolated mountain. *Tellus,* **32,** 348–364.

——, 1982: Synoptic observations and theory of orographically disturbed wind and pressure. *J. Atmos. Sci.,* **39,** 60–70.

——, 1988: Linear theory of hydrostatic flow over an isolated mountain in isosteric coordinates. *J. Atmos. Sci.,* **45,** 3889–3896.

——, 1989: Mountain-induced stagnation points in hydrostatic flow. *Tellus,* **41**(A), 270–274.

Somieski, F., 1981: Linear theory of three-dimensional flow over mesoscale mountains. *Beitr. Phys. Atmos.,* **54,** 315–334.

Stein, J., 1992: Contribution à l'étude des régimes hydrostatiques d'écoulement orographiqùes. Ph. D. thesis, Université Paul Sabatier, Toulouse, France, 243 pp. [Available from CNRM, Meteo France, 31057 Toulouse, France.]

Taylor, P. T., J. L. Walmsley, and J. R. Salmon, 1983: A simple model of neutrally stratified boundary layer flow over real terrain incorporating wavenumber-dependent scaling. *Bound.-Layer Meteor.,* **26,** 169–189.

Vergeiner, I., 1971: Operational linear lee wave model for arbitrary basic flow and two-dimensional topography. *Quart. J. Roy. Meteor. Soc.,* **97,** 30–60.

Wurtele, M., 1957: The three-dimensional lee wave. *Contrib. Atmos. Phys.,* **29,** 242–252.